



# Inhibiting phosphoglycerate dehydrogenase counteracts chemotherapeutic efficacy against *MYCN*-amplified neuroblastoma

Birte Arlt<sup>1,2,3,4</sup>  | Christin Zasada<sup>4</sup> | Katharina Baum<sup>5</sup> | Jasmin Wuenschel<sup>1,2</sup> | Guido Mastrobuoni<sup>4</sup> | Marco Lodrini<sup>1,2</sup> | Kathy Astrahantseff<sup>1</sup> | Annika Winkler<sup>1</sup> | Johannes H. Schulte<sup>1,3,6,7</sup> | Sabine Finkler<sup>1,2</sup> | Martin Forbes<sup>1,2,4</sup> | Patrick Hundsdoerfer<sup>1,8</sup> | Dennis Guergen<sup>9</sup> | Jens Hoffmann<sup>9</sup> | Jana Wolf<sup>5</sup> | Angelika Eggert<sup>1,3,6,7</sup> | Stefan Kempa<sup>4</sup> | Hedwig E. Deubzer<sup>1,2,3,6,7</sup> 

<sup>1</sup>Department of Pediatric Hematology and Oncology, Charité—Universitätsmedizin Berlin, Augustenburger Platz 1, 13353, Berlin, Germany

<sup>2</sup>Neuroblastoma Research Group, Experimental and Clinical Research Center (ECRC) of the Charité and the Max-Delbrück-Center for Molecular Medicine (MDC) in the Helmholtz Association, Lindenberger Weg 80, 13125, Berlin, Germany

<sup>3</sup>Berliner Institut für Gesundheitsforschung (BIH), Anna-Louisa-Karsch-Straße 2, 10178, Berlin, Germany

<sup>4</sup>Integrative Proteomics and Metabolomics, Berlin Institute for Medical Systems Biology at the Max-Delbrück Center for Molecular Medicine in the Helmholtz Association, Hannoversche Str. 28, 10115, Berlin, Germany

<sup>5</sup>Mathematical Modelling of Cellular Processes, Max-Delbrück Center for Molecular Medicine (MDC) in the Helmholtz Association, Robert-Rössle-Straße 10, 13125, Berlin, Germany

<sup>6</sup>German Cancer Consortium (DKTK), Partner Site Berlin, Berlin, Germany

<sup>7</sup>German Cancer Research Center (DKFZ), Heidelberg, Germany

<sup>8</sup>Department of Pediatric Oncology, Helios Klinikum Berlin Buch, Schwanebecker Chaussee 50, 13125, Berlin, Germany

<sup>9</sup>Experimental Pharmacology and Oncology Berlin-Buch GmbH (EPO), Robert-Rössle-Straße 10, 13125, Berlin, Germany

## Correspondence

Hedwig E. Deubzer, Charité –  
Universitätsmedizin Berlin, Department of  
Pediatric Hematology and Oncology,  
Augustenburger Platz 1, 13353 Berlin,  
Germany.  
Email: hedwig.deubzer@charite.de

## Funding information

Berlin Institute of Health, Grant/Award  
Numbers: 1.1.4.4, 53010045; Deutsche  
Krebshilfe, Grant/Award Numbers: 70112951,  
AVD 1233336; Deutsches Konsortium für  
Translationale Krebsforschung

## Abstract

Here we sought metabolic alterations specifically associated with *MYCN* amplification as nodes to indirectly target the *MYCN* oncogene. Liquid chromatography-mass spectrometry-based proteomics identified seven proteins consistently correlated with *MYCN* in proteomes from 49 neuroblastoma biopsies and 13 cell lines. Among these was phosphoglycerate dehydrogenase (PHGDH), the rate-limiting enzyme in de novo serine synthesis. *MYCN* associated with two regions in the *PHGDH* promoter, supporting transcriptional *PHGDH* regulation by *MYCN*. Pulsed stable isotope-resolved metabolomics utilizing <sup>13</sup>C-glucose labeling demonstrated higher de novo serine synthesis in *MYCN*-amplified cells compared to cells with diploid *MYCN*. An

**Abbreviations:** BCA, bichinonic acid assay; dTDP, deoxythymidine diphosphate; dTTP, deoxythymidine triphosphate; GC-MS, gas chromatography-mass spectrometry; LC-MS, liquid chromatography-mass spectrometry; LFQ, label-free quantification; PDX, patient-derived xenograft; PHGDH, phosphoglycerate dehydrogenase; PSAT1, phosphoserine aminotransferase 1; PSPH, phosphoserine phosphatase.

Stefan Kempa and Hedwig E. Deubzer contributed equally to this study.

This is an open access article under the terms of the Creative Commons Attribution-NonCommercial-NoDerivs License, which permits use and distribution in any medium, provided the original work is properly cited, the use is non-commercial and no modifications or adaptations are made.

© 2020 The Authors. *International Journal of Cancer* published by John Wiley & Sons Ltd on behalf of UICC.

independence of *MYCN*-amplified cells from exogenous serine and glycine was demonstrated by serine and glycine starvation, which attenuated nucleotide pools and proliferation only in cells with diploid *MYCN* but did not diminish these endpoints in *MYCN*-amplified cells. Proliferation was attenuated in *MYCN*-amplified cells by CRISPR/Cas9-mediated *PHGDH* knockout or treatment with *PHGDH* small molecule inhibitors without affecting cell viability. *PHGDH* inhibitors administered as single-agent therapy to NOG mice harboring patient-derived *MYCN*-amplified neuroblastoma xenografts slowed tumor growth. However, combining a *PHGDH* inhibitor with the standard-of-care chemotherapy drug, cisplatin, revealed antagonism of chemotherapy efficacy in vivo. Emergence of chemotherapy resistance was confirmed in the genetic *PHGDH* knockout model in vitro. Altogether, *PHGDH* knockout or inhibition by small molecules consistently slows proliferation, but stops short of killing the cells, which then establish resistance to classical chemotherapy. Although *PHGDH* inhibition with small molecules has produced encouraging results in other preclinical cancer models, this approach has limited attractiveness for patients with neuroblastoma.

#### KEYWORDS

cancer cell metabolism, cell death, de novo serine synthesis pathway, one-carbon metabolism, therapy resistance

## 1 | INTRODUCTION

Neuroblastoma is the most common extracranial solid malignancy of childhood,<sup>1</sup> and characterized by heterogeneous tumor biology producing dramatic clinical variability ranging from spontaneous regression or localized, stable disease to rapid metastasizing progression with fatal outcome.<sup>2</sup> Treatment protocols vary with this broad prognostic range, and spans observation or surgery alone to multimodal therapy in patients at high risk.<sup>3</sup> Multimodal therapy consists of induction therapy delivering at least seven different chemotherapeutic drugs, primary tumor resection, high-dose myeloablative chemotherapy followed by autologous or haploidentical stem cell rescue and local radiation of the primary tumor bed and, potentially, any remaining metabolically active, morphologically identifiable distant metastases.<sup>3,4</sup> Independent of conditioning regimen and source of stem cell graft, all patients receive consolidation therapy composed of at least 5 cycles of the ch14.18 chimeric antibody directed against the GD2 disialoganglioside expressed on the neuroblastoma cell surface.<sup>5</sup> The number of long-term survivors of high-risk disease has remained unsatisfactorily poor despite the ~18 months necessary for this therapy to reach its maximum tolerable toxicity. Survival is as low as 40% after first-line therapy and <10% after relapse,<sup>6</sup> necessitating identification of truly novel druggable molecular mechanisms.

That molecular features determine neuroblastoma aggressiveness and risk for relapse is well documented,<sup>6</sup> adding *MYCN* amplifications<sup>7</sup> and activating *TERT* rearrangements<sup>8</sup> to the clinical risk factors (>18 months of age at diagnosis and INRG stage M<sup>2</sup>). *MYCN* amplification plays a key role in neuroblastoma pathogenesis, and was first described in 1983.<sup>10</sup> The *MYCN* gene is localized to chromosome 2p24.3, and encodes a 64 kDa nucleoprotein that both activates and represses large sets of target genes.<sup>11-13</sup>

### What's new?

Molecular alterations in neuroblastoma influence disease aggressiveness and relapse risk. In particular, molecular amplification of the oncogene *MYCN* is a major determinant of patient outcome. Here, shotgun proteomics was combined with metabolomics to investigate alterations in *MYCN* as potential therapeutic targets in neuroblastoma. A strong correlation was detected between *MYCN* amplification and proteins involved in serine synthesis, including the rate-limiting enzyme *PHGDH*, and one-carbon metabolism. Targeting *PHGDH* by genetic knockout and small molecule inhibitors stalled proliferation but did not kill neuroblastoma cells. Chemotherapeutic resistance was evident in mice with patient-derived neuroblastoma xenografts following treatment with *PHGDH* inhibitors and cisplatin.

Approximately 20% of all neuroblastomas are driven by high-level *MYCN* amplifications. While *MYCN*-amplified tumors respond well initially to therapy, they demonstrate more aggressive features at diagnosis and more progress during induction treatment, translating into lower patient survival after progression or relapse.<sup>14</sup> While directly targeting *MYCN* remains a challenge due to its nuclear localization, lack of ligand binding site and diverse physiological functions for normal tissue maintenance,<sup>15</sup> indirect approaches targeting binding partners or downstream effectors yield encouraging results. We here set out to identify metabolic alterations specifically associated with *MYCN* amplification as novel targets.

## 2 | MATERIALS AND METHODS

### 2.1 | Characteristics of patients and tumor samples

Tumor samples from 49 neuroblastoma patients, constituting a representative neuroblastoma cohort (Supporting Information Table S1), were collected internationally between 1989 and 2015 and had tumor cell counts ranging from 50% to 90%. Formalin-fixed, paraffin-embedded samples from 80 primary neuroblastomas (48 localized or INSS stage 4S and 32 stage 4 with 7 harboring *MYCN* amplifications) available from patients in the NB2014 trial (informed consent available) were selected for PHGDH immunohistochemistry.

### 2.2 | Animal experiments

The patient-derived *MYCN*-amplified neuroblastoma xenograft 14647 generated within the IMI2 ITCC-P4 consortium (informed patient consent available from consortium) was serially transplanted in mice at least three times prior to subcutaneous implantation in the flanks of 8-week-old female NOG mice ( $n = 4$  per study group) for these experiments. Mice were randomly assigned to six groups after tumor volumes reached  $100 \text{ mm}^3$ . Three study groups received single-agent treatment with either cisplatin (1 mg/kg iv once weekly) or the PHGDH inhibitors, NCT-503 (40 mg/kg/d ip) or PKUMDL-WQ-2101 (20 mg/kg/d ip). Two study groups received the combinations of one PHGDH inhibitor together with cisplatin (drugs administered in the same schedules as in the single-agent study arms) and one group received the combined vehicle control (0.1 mL 0.9% NaCl iv once weekly and 0.2 mL 10% DMSO and 0.1 mL 0.1% Tween-20 ip once daily). Mice in single- or double-treatment arms also received vehicle for the drug(s) that they were not receiving for a uniform background. Tumor size was measured every 3 days using a caliper. Tumor volume was calculated using the formula  $(\text{breadth} \times \text{length} \times \text{height})/2$ . Mice were treated for maximally 25 days and euthanized by cervical dislocation when tumor size exceeded  $1500 \text{ mm}^3$ .

### 2.3 | Cell culture

The BE(2)-C (also called SK-N-BE(2)-C (RRID: CVCL\_0529) was obtained from ECACC (Salisbury, UK) and the IMR-32 (RRID: CVCL\_0346), Kelly (RRID: CVCL\_2092), GI-ME-N (RRID: CVCL\_1232) and SH-SY5Y (RRID: CVCL\_0019) cell lines from the DSMZ (Braunschweig, Germany). CLB-GA (RRID: CVCL\_9529), IMR5/75 (RRID: CVCL\_M473), subclone of IMR-32 (RRID: CVCL\_0346) and LAN-6 (RRID: CVCL\_1363) cell lines were kindly provided by M. Fischer (University Hospital Cologne), the NB-1 (RRID: CVCL\_1440) cell line by I. Oehme (DKFZ, Heidelberg), the SK-N-AS (RRID: CVCL\_1700), SK-N-DZ (RRID: CVCL\_1701) and SK-N-SH (RRID: CVCL\_0531) cell lines by J. Schulte (Charité, Berlin) and the CHP-134 (RRID: CVCL\_1124), NGP (RRID: CVCL\_2141), NLF (RRID: CVCL\_E217), LAN-1 (RRID: CVCL\_1827) and SH-EP (RRID:

CVCL\_0524; epithelial-like subclone of SK-N-SH) cell lines by L. Savelyeva (DKFZ, Heidelberg). Cell lines were maintained at  $37^\circ\text{C}$  and 5%  $\text{CO}_2$  in DMEM (Thermo Fisher Scientific) medium lacking glucose, glutamine, sodium pyruvate and phenol red and supplemented with 10% fetal calf serum (Merck), 2.5 g/L glucose (Merck) and 2 mM glutamine (Thermo Fisher Scientific). A modified DMEM version lacking only serine and glycine and containing the same supplements was used in starvation experiments. The synthetic *MYCN*-inducible SH-EP Tet-21/N off model was maintained as described.<sup>16</sup> The *MYCN*-inducible SH-SY5Y Tet-21/N on model provided by F. Westermann (DKFZ, Heidelberg) was cultured with 0.2  $\mu\text{g}/\text{mL}$  G418 (Merck), 7.5  $\mu\text{g}/\text{mL}$  blasticidin (Merck) and treated with 1  $\mu\text{g}/\text{mL}$  tetracycline (Merck) to induce synthetic *MYCN* expression. IMR-32 cells stably transfected with a tetracycline-inducible *MYCN* shRNA expression system (IMR32-6TR-MYCNsh) were kindly provided by F. Westermann (DKFZ, Heidelberg) and cultured in DMEM with 10% FCS and 1% NEAA supplemented with 250  $\mu\text{g}/\text{mL}$  Zeocin (Invitrogen) and 5  $\mu\text{g}/\text{mL}$  blasticidin. Cells were treated with 1  $\mu\text{g}/\text{mL}$  tetracycline (AppliChem, Darmstadt, Germany) to induce sh*MYCN* expression. Cell lines were authenticated using high-throughput SNP-based assays<sup>17</sup> within the last 3 years and regularly monitored for mycoplasma using Plasmotest (InvivoGen) according to the manufacturer's instructions. All experiments were performed with mycoplasma-free cells. The following cell lines ( $n = 13$ ) were used for LC-MS-based shotgun proteomics: BE(2)-C, IMR-32, Kelly, GI-ME-N, SH-SY5Y, LAN-6, SK-N-DZ, SK-N-SH, NGP, LAN-1, SH-EP, SH-EP Tet-21/N and SH-SY5Y Tet-21/N. Protocols to generate CRISPR/Cas9-mediated PHGDH knockout clones, qRT-PCR, ChIP qPCR, western blotting, tumor immunohistochemistry, assays for proliferation, colony formation and flow cytometry are supplied in the Supporting Information Materials and Methods.

### 2.4 | Tumor and cell line proteome discovery

Proteins were extracted from tumor samples in urea buffer (8 M urea, 100 mM Tris-HCl, pH 8.25) containing zirconium beads (Roth) with mechanical disruption (twice) at 6500 oscillation  $\text{min}^{-1}$  for 20 seconds using a Precellys 24 homogenizer (Bertin Technologies). Cell debris and beads were removed by centrifugation at 20 000g for 3 minutes, then protein concentrations determined by bicinchoninic acid assay (BCA) assay. Proteins were extracted from pelleted cells from cell lines in urea buffer without mechanical disruption before isolating and assessing protein content as for tumor samples. In total, 50  $\mu\text{g}$  tumor-derived protein and 100  $\mu\text{g}$  cell line-derived protein were prepared (Supporting Information Materials and Methods) for liquid chromatography-mass spectrometry (LC-MS)-based proteomics as previously described.<sup>18</sup> Desalted and purified peptide mixtures were analyzed in duplicate on a NanoLC400 (Eksigent) coupled to Q Exactive HF tandem mass spectrometer (Thermo Fisher Scientific) in a shotgun proteomics approach (detailed in the Supporting Information Materials and Methods). Data acquisition was performed in a data-dependent mode with one survey MS scan (resolution of 120 000 at 200 m/z) followed by a

maximum of 10 MS/MS scans (resolution of 30 000 at 200 m/z) with an intensity threshold of 5000 for the most intense ions. Fragmented ions were automatically excluded from further selection for 45 seconds to improve acquisition of low-abundant ions. Raw data were analyzed using the MaxQuant proteomics pipeline (version 1.5.3.30) with the human Uniprot database (38 538 protein entries, May 2013 download) and a common contaminants database (245 protein entries).<sup>19</sup> Cysteine carbamidomethylation was set as a fixed modification in analysis settings, while methionine oxidation and N-terminal acetylation were set as variable modifications. Two missed cleavage sites were allowed, and peptide tolerance was set to 7 ppm. A 1% false-discovery rate was applied to filter search engine peptide assignments. Other parameters used default settings. Quality control was performed as described.<sup>20</sup> Further data analyses were performed with Perseus version 1.6.0.2.<sup>21,22</sup> Reverse and contaminant entries were removed, and label-free quantification (LFQ) values were logarithmized. Proteins with valid LFQ values in at least 35% of tumor or cell line samples were included in further analyses. If valid LFQ values were available in <2 technical replicates for a tumor biopsy or <2 biological replicates for a cell line, values were set to *not available*. LFQ values for each protein were independently averaged among tumor biopsies and cell lines for Spearman correlation coefficient calculation. Data were visualized using R studio version 1.1.463 and R version 3.5.1.<sup>23</sup>

## 2.5 | Metabolomics

Medium was changed 24 and 4 hours before harvesting cells for metabolome capture using pulsed stable isotope-resolved metabolomics in tandem with absolute quantitative gas chromatography (GC)-MS. Labeling with stable isotopes was accomplished by medium change 10 minutes before harvest to medium containing either 2.5 g/L <sup>13</sup>C-glucose or 2.5 g/L <sup>12</sup>C-glucose, the latter representing the natural mass isotopic distribution. Harvested cells were washed with HEPES buffer (140 mM NaCl, 5 mM HEPES, pH 7.4) containing labeled or nonlabeled glucose and quenched by adding 50% ice-cold methanol containing 2 µg/mL cinnamic acid (Merck) as an internal control. Polar metabolites were extracted as previously described<sup>24</sup> (Supporting Information Materials and Methods) from cell samples, then split for nucleotide pool quantification and absolute metabolite quantification on a Pegasus IV-ToF-MS-System (LECO) complemented with an autosampler (MultiPurpose Sampler 2 XL, Gerstel). Samples were injected in 1:5 split mode in a 1 µL injection volume (temperature-controlled CAS4 injector with a baffled glass liner). The initial temperature of 80°C (30 seconds), was ramped 120°C (12°C/min) then to 300°C (7°C/min) where it was held for 120 seconds. Gas chromatographic separation was performed on an Agilent 78903 (Agilent Technologies) equipped with a VF-5 MS column (30 m length, 250 µm inner diameter, 0.25 µm film thickness) and helium as a carrier gas (flow rate = 1.2 mL/min) with an initial temperature of 70°C (120 seconds) ramped to 120°C (5°C/min) then to 350°C (7°C/min) where it was held for 120 seconds. Spectra were measured at 20 spectra/sec in the mass range of m/z = 60-600 mass units (detector voltage = 1650 V). GC-MS

chromatograms were processed using ChromaTOF version 4.51.6.0 (LECO). Retention times were normalized using alkane retention times and Kovats retention index.<sup>25</sup> Mass spectra and mass isotopomer distributions were extracted from ChromaTOF using MetMax version 1.0.1.12 (MPIMP GoIm)<sup>24</sup> or MAUI-VIA version 1.0.5.<sup>26</sup> Acquired data were normalized to the internal control cinnamic acid and calculated in pmol/million cells (Supporting Information Data).

## 2.6 | Nucleotide pool quantification

Intracellular nucleotide pools were quantified in cell lines from extracted polar metabolites using direct-infusion MS. Sample preparation was previously described<sup>27</sup> and is detailed in the Supporting Information Materials and Methods. Desalted prepared samples were analyzed on a TSQ Quantiva triple quadrupole mass spectrometer (Thermo Scientific) coupled to a Triversa Nanomate (Advion) ion source (spray voltage = 1.5 kV, head gas pressure = 0.5 psi). Argon was used as collision gas (pressure = 1.5 mTorr). Full width as half maximum resolutions for Q1 and Q3 were set as 0.7. Data acquisition ran 3 minutes per sample (cycle time = 3.3 seconds) with total acquisition from 55 selected reaction monitoring scans for each nucleotide. The sum of the two best transitions for each nucleotide were acquired in negative mode. Data were processed using Xcalibur version 4.0.27.13 (Thermo Fisher Scientific) and an OpenMS package, and were visualized with R studio version 1.1.463 and R version 3.5.1.<sup>23</sup> Calibration standards controlled for a valid quantification range above the signal-to-noise threshold.

## 2.7 | Statistical analysis

Global proteome profiles were correlated with corresponding MYCN expression levels in a Spearman ranks test using the Hmisc package version 4.3-0. MYCN expression levels based on tumor biopsy FISH (provided by the German Neuroblastoma Biobank), western blotting for synthetic inducible MYCN systems and digital droplet PCR for cell lines<sup>28</sup> were transformed to scores ranging between -5 (diploid MYCN status) and 5 (highest MYCN expression measured in all tumor samples or cell lines). Scores were aligned after manual data assessment (Supporting Information Data). T-tests tested the null hypothesis of zero correlation, the Benjamini-Hochberg method corrected for multiple testing,<sup>29</sup> and normalized label-free protein quantities with corrected P-values <.05 were regarded as significantly correlated with the MYCN score. The first gene name associated to a protein was used for overlap computations, and duplicated gene names were distinguished by their majority protein IDs. The overlap prediction was robust when all gene names associated with a protein were included. Statistical analysis was performed using GraphPad Prism version 7 and R studio version 1.1.463 with R versions 3.5.1<sup>23</sup> and 3.6.1.<sup>30</sup> If not otherwise stated, a two-tailed Student's t-test with Welch's correction was applied to test significance of differences between testing groups.

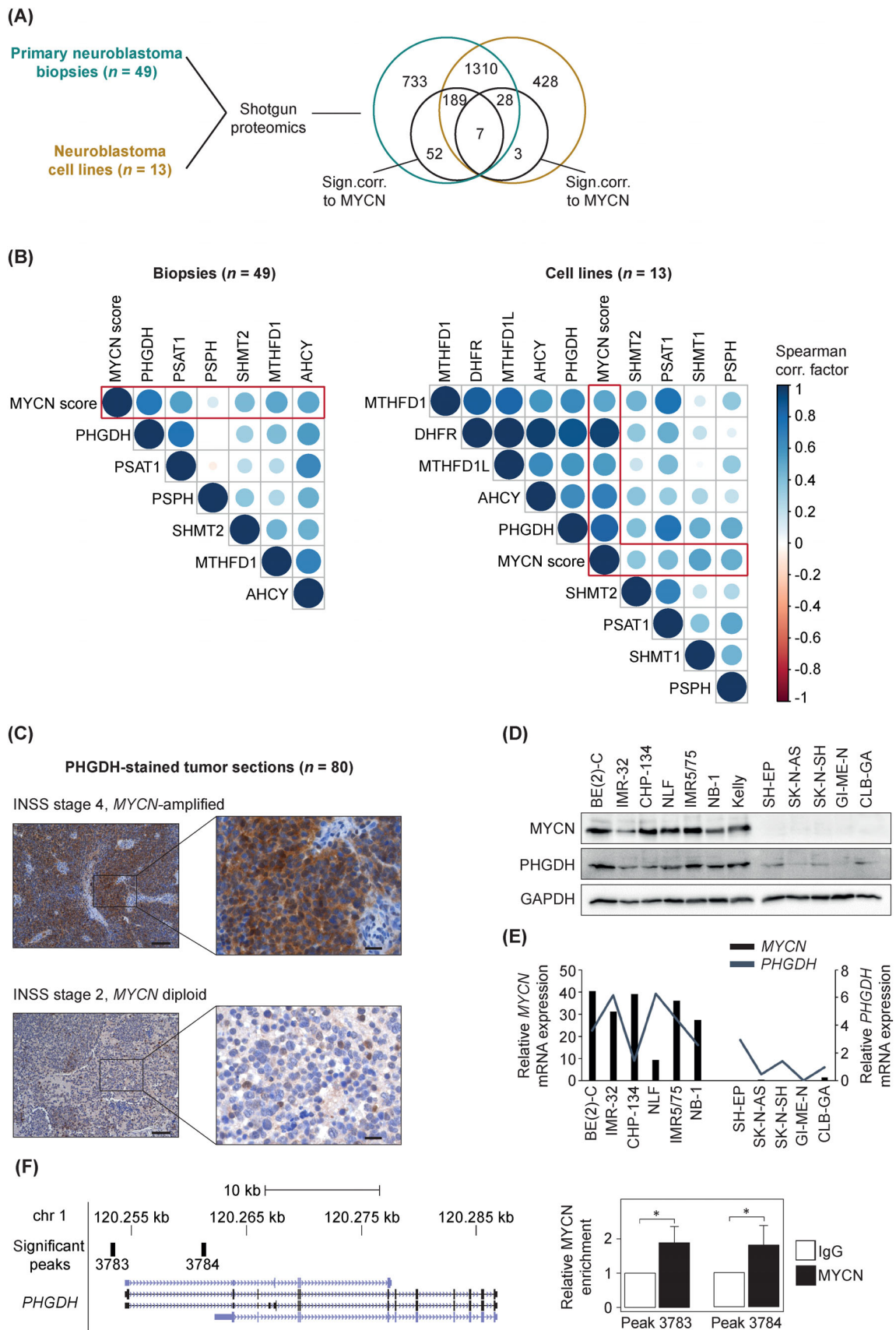


**FIGURE 1** Legend on next page.

**TABLE 1** Overview of proteins correlating with MYCN expression scores in both neuroblastoma biopsies and cell lines

Protein	Tumor biopsies (n = 49)		Cell lines (n = 13)	
	Spearman rank correlation coefficient	P-value <sup>a</sup>	Spearman rank correlation coefficient	P-value <sup>a</sup>
PHGDH	0.7126	.0014	0.8367	.0245
SERPINB6	-0.5845	.0015	-0.8803	.0298
PEA15	-0.5391	.0046	-0.8682	.0163
LUC7L	0.5126	.0122	0.8098	.0352
HNRNPAB	0.4538	.0191	0.7637	.0476
TAGLN2	-0.4187	.0343	-0.7727	.0467
CAP1	-0.406	.0429	-0.8319	.0245

<sup>a</sup>P-value corrected for multiple testing according to the Benjamini-Hochberg method.<sup>29</sup>

### 3 | RESULTS

#### 3.1 | Oncogenic MYCN levels promote PHGDH expression in neuroblastoma cells

To decipher metabolic mechanisms controlled by MYCN that have remained enigmatic, protein expression was quantified in a representative cohort of 49 primary neuroblastoma biopsies (Supporting Information Table S1) and panel of 13 neuroblastoma cell lines using LC-MS-based shotgun proteomics. The expression of 248 proteins (2319 quantified in total) in tumors and 38 proteins (1965 quantified in total) in cell lines significantly correlated with MYCN expression (Figure 1A). Among these, phosphoglycerate dehydrogenase (PHGDH) and 6 other proteins correlated with MYCN expression scores in both models (Figure 1A, Table 1). Spearman correlation analysis independently identified PHGDH as most strongly correlating with the MYCN score (Spearman rank correlation coefficient  $r_s = 0.71$  for tumor biopsies and  $r_s = 0.84$  for cell lines; Table 1). High-level MYCN expression in neuroblastomas and cell lines also strongly correlated with other proteins involved in de novo serine synthesis and one-carbon metabolism (Figure 1B). To assess whether differential PHGDH expression in the context of varying MYCN status is mirrored at the cellular level, PHGDH expression was immunohistochemically assessed in 80 selected samples from tumors with the most divergent characteristics. PHGDH was strongly expressed in the cytoplasm of nearly all cells in MYCN-amplified tumors (median score = 12, first quartile 4.5, third quartile 12), whereas little or no

PHGDH expression was detected in any tumor lacking MYCN amplification (median score = 0, first quartile 0, third quartile 4;  $P < .0001$ ; Figure 1C). Reanalysis of existing transcriptomic data from a panel of 643 primary neuroblastomas demonstrated a strong differential PHGDH expression among MYCN single vs MYCN-amplified tumors already at the level of mRNA expression (Supporting Information Figure S1A). Western blotting verified PHGDH expression in the panel of cell lines derived from neuroblastomas harboring or lacking MYCN amplifications. PHGDH in cell lines reflected the higher PHGDH expression in MYCN-amplified cells also observed in primary tumors (Figure 1D). PHGDH transcripts were up to 40-fold more abundant in qRT-PCR analysis of MYCN-amplified, as compared to diploid MYCN cell lines (Figure 1E). Inducing MYCN in the synthetic MYCN-inducible SH-EP Tet-21/N model enhanced PHGDH expression on protein level (Supporting Information Figure S1B). MYCN depletion after MYCN knockdown in stably transfected IMR-32 cells with a tetracycline-inducible MYCN shRNA expression system decreased PHGDH protein expression (Supporting Information Figure S1C). Two MYCN recruitment sites in the PHGDH promoter were reported in existing ChIP-Seq data from SK-N-BE(2)-C cells<sup>31</sup> (Figure 1F), and ChIP qPCR using this cell line showed an ~2-fold enrichment of PHGDH promoter DNA associated with MYCN over IgG at both sites, supporting a role for MYCN in the transcriptional activation of PHGDH in neuroblastoma cells (Figure 1F). Our data strongly correlates oncogenic MYCN expression driven by gene amplification in neuroblastoma with high-level expression of PHGDH and other proteins involved in serine synthesis and one-carbon metabolism.

**FIGURE 1** PHGDH belongs to a protein set correlating most strongly with MYCN expression. A, Venn diagram shows the number of proteins whose absolute abundance in tumor samples and cell lines (and the intersection of both) significantly correlate with MYCN score. B, Color intensity and size in circles represents Spearman correlation factors (after hierarchical clustering in dataset described in A) to identify proteins also correlated with MYCN score that are involved in serine synthesis and one-carbon metabolism. C, PHGDH immunohistochemical staining (brown) is exemplarily shown from one high-risk MYCN-amplified neuroblastoma and one low-risk neuroblastoma (diploid MYCN). Sizing bars correspond to 100  $\mu\text{m}$  (left) and 20  $\mu\text{m}$  (right). MYCN and PHGDH expression in cell lines was confirmed on protein (D) and mRNA (E) levels using western blotting and qRT-PCR, respectively. Fold-changes above arithmetic means for MYCN and PHGDH are shown for qRT-PCR, and samples were normalized using the  $\Delta\Delta\text{Ct}$  method and the *HPRT* and *SDHA* housekeeping gene(s). GAPDH was used as a loading control in western blotting. F, Positions of the two previously identified MYCN-binding regions in the PHGDH promoter (schematic model based on the GRCh37/hg19 UCSC genome browser) are indicated by vertical lines showing enrichment locations of ChIP-Seq data peaks, 3783 and 3784<sup>31</sup> on chromosome 1 (chr 1). Blue horizontal lines indicate PHGDH transcript variants. MYCN recruitment to PHGDH promoter sequences corresponding to peaks 3783 and 3784 was confirmed by ChIP qPCR in which BE(2)-C cell lysates were immunoprecipitated with antibodies against MYCN or IgG (negative control). Bars (right graphic) show mean fold-changes over IgG  $\pm$  SD (n = 4). \* $P < .05$

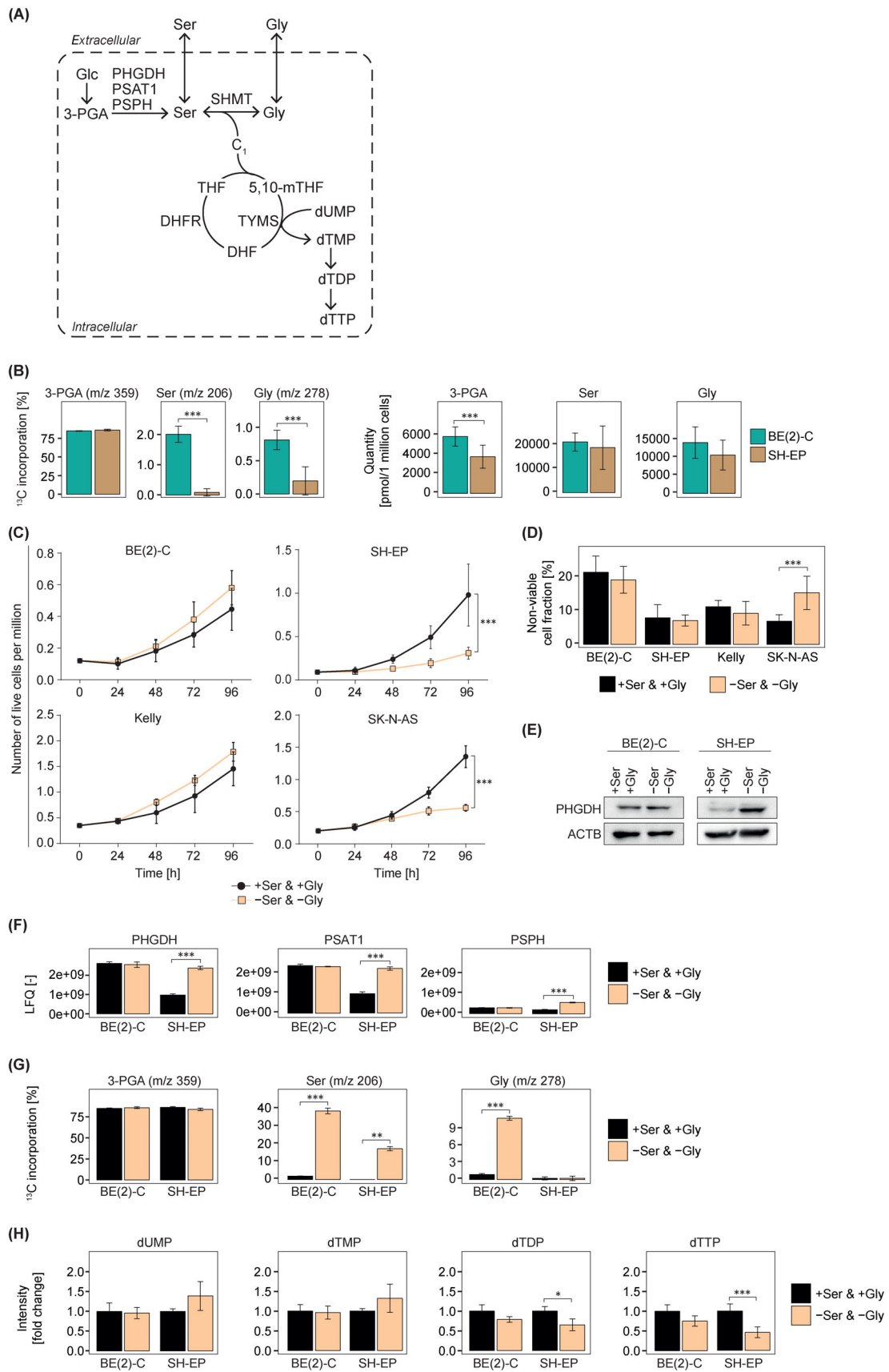


**FIGURE 2** Legend on next page.

### 3.2 | MYCN amplification makes neuroblastoma cells independent from exogenous serine and glycine import

Serine biosynthesis, using the glycolytic intermediate 3-phosphoglycerate, is a side branch of glucose metabolism. Serine is a precursor for glycine and cysteine amino acid biosynthesis as well as contributing single carbons to one-carbon metabolism for nucleotide synthesis, among other roles.<sup>32,33</sup> Since PHGDH catalyzes the rate-limiting step in serine synthesis (Figure 2A), we performed metabolic flux analyses in neuroblastoma cells to investigate the functional consequences of MYCN-induced enhancement of PHGDH expression. Carbon usage was traced through serine synthesis in BE(2)-C (MYCN-amplified) and SH-EP (MYCN diploid) cells using pulsed labeling with <sup>13</sup>C-glucose (vs <sup>12</sup>C-glucose control) followed by quantitative metabolomics. Both cell lines comparably incorporated glucose-derived carbons into 3-phosphoglycerate, while total 3-phosphoglycerate levels were 1.5-fold higher in BE(2)-C cells. Label incorporation into serine and glycine was 5- to 10-fold higher in BE(2)-C cells while total serine and glycine levels remained similar in both cell lines (Figure 2B). Similar label incorporation into 3-phosphoglycerate, serine and glycine were obtained in a second MYCN nonamplified cell line, SH-SY5Y, thus confirming the previous finding in SH-EP cells (Supporting Information Figure S2). We tested whether cellular PHGDH levels altered their capacity to compensate for exogenous serine and glycine deprivation. Proliferation and viability of MYCN-amplified BE(2)-C and Kelly cell lines were not statistically different if cultured in serine- and glycine-depleted or full medium (Figure 2C,D). SH-EP and SK-N-AS (both diploid) cell proliferation was diminished by 2- to 3-fold by serine and glycine depletion (Figure 2C), which was accompanied by a ~3-fold increase in the nonviable SK-N-AS cell fraction (Figure 2D). Western blotting, shotgun proteomics and metabolomics were used to comparatively examine the impact of serine and glycine deprivation in BE(2)-C and SH-EP cells on enzymes, intermediates and products in serine synthesis and on intracellular pyrimidine nucleotide pools. While PHGDH, phosphoserine aminotransferase 1 (PSAT1) and phosphoserine phosphatase (PSPH) expression levels in BE(2)-C cells remained unchanged by serine and glycine starvation, all three

proteins were upregulated in SH-EP cells (Figure 2E,F). Label incorporation into 3-phosphoglycerate was comparable in both cell lines under normal or serine- and glycine-starved conditions, whereas significantly higher glucose-derived <sup>13</sup>C was incorporated into serine and glycine in starved BE(2)-C compared to SH-EP cells (Figure 2G). These data demonstrate that the high PHGDH levels in BE(2)-C cells better compensate for exogenous serine and glycine depletion than low PHGDH levels in SH-EP cells. The low PHGDH levels in SH-EP cells were capable of increasing serine synthesis, but only to levels about half of those in BE(2)-C cells, but no increase in labeled glycine was detected (Figure 2G). This lack of efficient conversion of serine to glycine demonstrates that one-carbon metabolism is limited in SH-EP cells. As rapidly proliferating cancer cells require single carbons for nucleotide synthesis, we investigated whether this limited carbon flow into one-carbon metabolism reduced pyrimidine nucleotide pools in BE(2)-C and SH-EP cells. Deoxythymidine diphosphate (dTDP) and deoxythymidine triphosphate (dTTP) levels were lower in SH-EP cells under serine- and glycine-starved conditions, while pyrimidine nucleotide pools were unaltered in BE(2)-C cells (Figure 2H). We conclude that the ability of MYCN-amplified neuroblastoma cells to ramp up PHGDH levels make them independent of an exogenous serine and glycine supply.

### 3.3 | Targeting PHGDH alone in neuroblastoma models has minor long-term efficacy and antagonizes standard chemotherapy success

To investigate whether high PHGDH levels in BE(2)-C cells support the uncoupled proliferation that is a cancer hallmark, proliferation and viability were monitored in single-cell PHGDH knockout clones generated using CRISPR/Cas9 and validated at the protein and metabolome levels (Figure 3A,B). Depleting PHGDH expression reduced proliferation in all clones by ~80% compared to control cells, while the nonviable cell fraction was only marginally increased in three clones and unaltered in the remaining two clones (Figure 3C). These data demonstrate that the majority of BE(2)-C cells can adapt to the loss of the rate-limiting enzyme in serine synthesis and remain viable. Having shown that

**FIGURE 2** MYCN amplification releases neuroblastoma cell dependency on exogenous serine and glycine for proliferation. A, Schematic representation of serine synthesis and one-carbon metabolism. B, Cells were cultured for 48 hours and pulsed with medium containing fully labeled <sup>13</sup>C- or <sup>12</sup>C-glucose for 10 minutes before harvest for quantitative metabolomics. Bars represent percentages of <sup>13</sup>C-label incorporation into the indicated molecules (left) and their absolute quantities per 1 million cells (right). Number of live (C) and nonviable (D) cells grown in full (black) or serine- and glycine-depleted (tan) medium. Bars represent the mean (±SD) fraction size of nonviable cells at 96 hours (n = 3). E, Western blot analysis of PHGDH expression in BE(2)-C and SH-EP cells grown for 48 hours in full (left bands) or serine- and glycine-depleted (right bands) medium. β-Actin served as loading control. F, Quantified PHGDH, PSAT1 and PSPH levels in BE(2)-C and SH-EP cells grown 48 hours in full (black) or serine- and glycine-depleted (tan) medium. Bars represent mean ± SD (n = 3). G, Percentage of <sup>13</sup>C label incorporation into indicated molecules in BE(2)-C and SH-EP cells grown 48 hours in full (black) or serine- and glycine-depleted (tan) medium. Bars represent mean ± SD (n = 3). H, Pyrimidine nucleotide levels in BE(2)-C and SH-EP cells grown for 48 hours in full (black) or serine- and glycine-depleted (tan) medium. Bars show mean fold-changes (± SD, n ≥ 4) compared to nonstarved cells. \*P < .05; \*\*P ≤ .01; \*\*\*P ≤ .001. C1, one-carbon unit; DHF, dihydrofolate; DHFR, dihydrofolate reductase; Glc, glucose; Gly, glycine; 5,10-mTHF, 5,10-methylenetetrahydrofolate; 3-PGA, 3-phosphoglycerate; PSAT1, phosphoserine aminotransferase 1; PSPH, phosphoserine phosphatase; Ser, serine; SHMT, serine hydroxymethyltransferase; THF, tetrahydrofolate; TYMS, thymidylate synthase; dUMP, deoxyuridine monophosphate; dTMP, deoxythymidine monophosphate; dTDP, deoxythymidine diphosphate; dTTP, deoxythymidine triphosphate. LFQ, label-free quantification



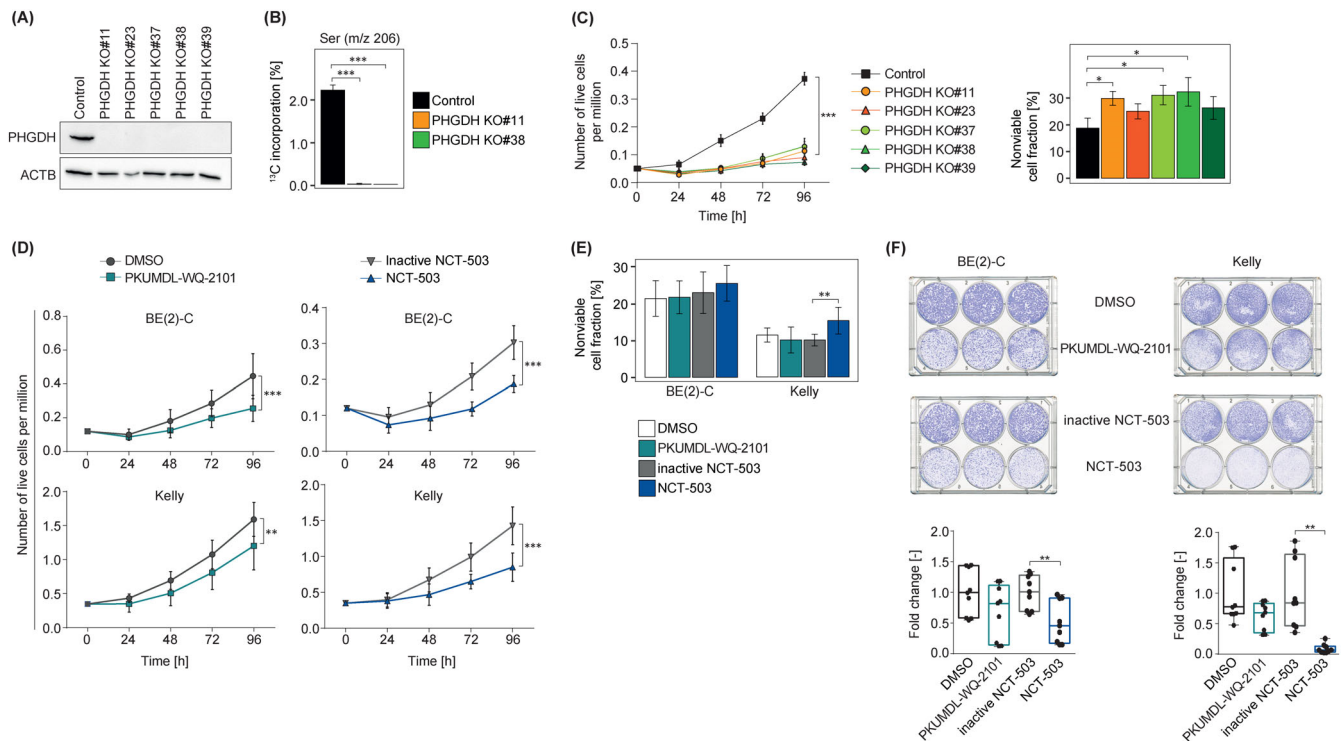


**FIGURE 3** PHGDH knockout and small molecule drug inhibition slows neuroblastoma cell proliferation and inhibits colony formation. A, Western blot analysis of PHGDH expression in CRISPR/Cas9-mediated PHGDH knockout clones and respective BE(2)-C control cells. β-Actin served as loading control. B, Bars show glucose-derived <sup>13</sup>C incorporation into serine in PHGDH knockout clones and control cells grown for 48 hours in full medium (mean ± SD, n = 3). C, Numbers of live and nonviable PHGDH knockout and control cells were assessed up to 96 hours after seeding. Plotted data points and bars represent mean ± SD (n = 3, nonviable cell fraction determined at 96 hours). Numbers of live (D) and fraction of nonviable (E) BE(2)-C and Kelly cells treated singly with 10 μM PKUMDL-WQ-2101, 10 μM NCT-503 or solvent control for 96 hours are shown. Plotted data points and bars represent mean ± SD (n = 3). F, BE(2)-C and Kelly cells were seeded at low density, then treated with 10 μM PKUMDL-WQ-2101 (or DMSO control) or 10 μM NCT-503 (or inactive drug control). Cell colonies were stained with crystal violet after 9 days of treatment (photographs) with box-and-whisker plots (below photographs) presenting median fold-changes in colony quantification relative to vehicle control (from Image J software, n ≥ 3). \*P < .05, \*\*P < .01, \*\*\*P < .001

MYCN regulates serine synthesis and one-carbon metabolism in neuroblastoma cells and that CRISPR/Cas9-induced depletion of PHGDH suppresses proliferation, we turned to the commercially available PHGDH inhibitors, PKUMDL-WQ-2101<sup>34</sup> and NCT-503<sup>35</sup> (chemical structures shown in Supporting Information Figure S3), to test the therapeutic potential of targeting PHGDH as an indirect method to target oncogenic MYCN in neuroblastoma models. Semiautomated trypan blue staining was used to monitor both viability and proliferation in MYCN-amplified cell lines. The two structurally divergent small molecule PHGDH inhibitors equally reduced proliferation by approximately 30% (Figure 3D) without sustainably inducing cell death (Figure 3E). Cell cycle analysis demonstrated a consistent G<sub>0</sub>/G<sub>1</sub> cell cycle arrest by PKUMDL-WQ-2101 and NCT-503 treatment in BE(2)-C and Kelly cells, respectively (Supporting Information Figure S4). Colony formation capacity was also suppressed by PKUMDL-WQ-2101 and NCT-503 treatment by 2- to 3-fold (Figure 3F). Altogether, pharmaceutically targeting PHGDH exerted moderate tumor-suppressive effects in MYCN-amplified cell lines in vitro.

We turned to our panel of eight patient-derived neuroblastoma xenografts (PDXs) to assess inhibitor efficacy in mouse models.

Western blotting confirmed a strong correlation between high-level MYCN and PHGDH expression in the PDXs (Figure 4A). PDX 14647 was selected for further experiments because it is characterized by strong PHGDH expression combined with high tumor take rates in serial transplantation. PKUMDL-WQ-2101 and NCT-503 treatment regimens were well tolerated without causing weight loss or obvious signs of toxicity. No alterations in physical status or behavior of the mice were observed. After short-term treatment for 10 days with either PHGDH inhibitor, PDX 14647 tumor volumes were 1.3- to 2-fold smaller compared to vehicle-treated mice (mean tumor volumes: 282 mm<sup>3</sup>, PKUMDL-WQ-2101; 429 mm<sup>3</sup>, NCT-503; 563 mm<sup>3</sup>, vehicle; Figure 4B, Supporting Information Figure S5). After longer-term treatment for 25 days, mean tumor volume progressed only to 1371 mm<sup>3</sup> in PKUMDL-WQ-2101-treated mice compared to 1661 mm<sup>3</sup> mean tumor volume in vehicle-treated mice (Figure 4B). PDX growth remained altogether unaffected in mice treated with NCT-503 for 25 days, with a final mean tumor volume of 1639 mm<sup>3</sup> after NCT-503 monotherapy compared to the 1661 mm<sup>3</sup> mean tumor volume in vehicle-treated mice (Figure 4B). Based on RECIST criteria,<sup>36</sup> the longer-term monotherapy with PKUMDL-WQ-2101

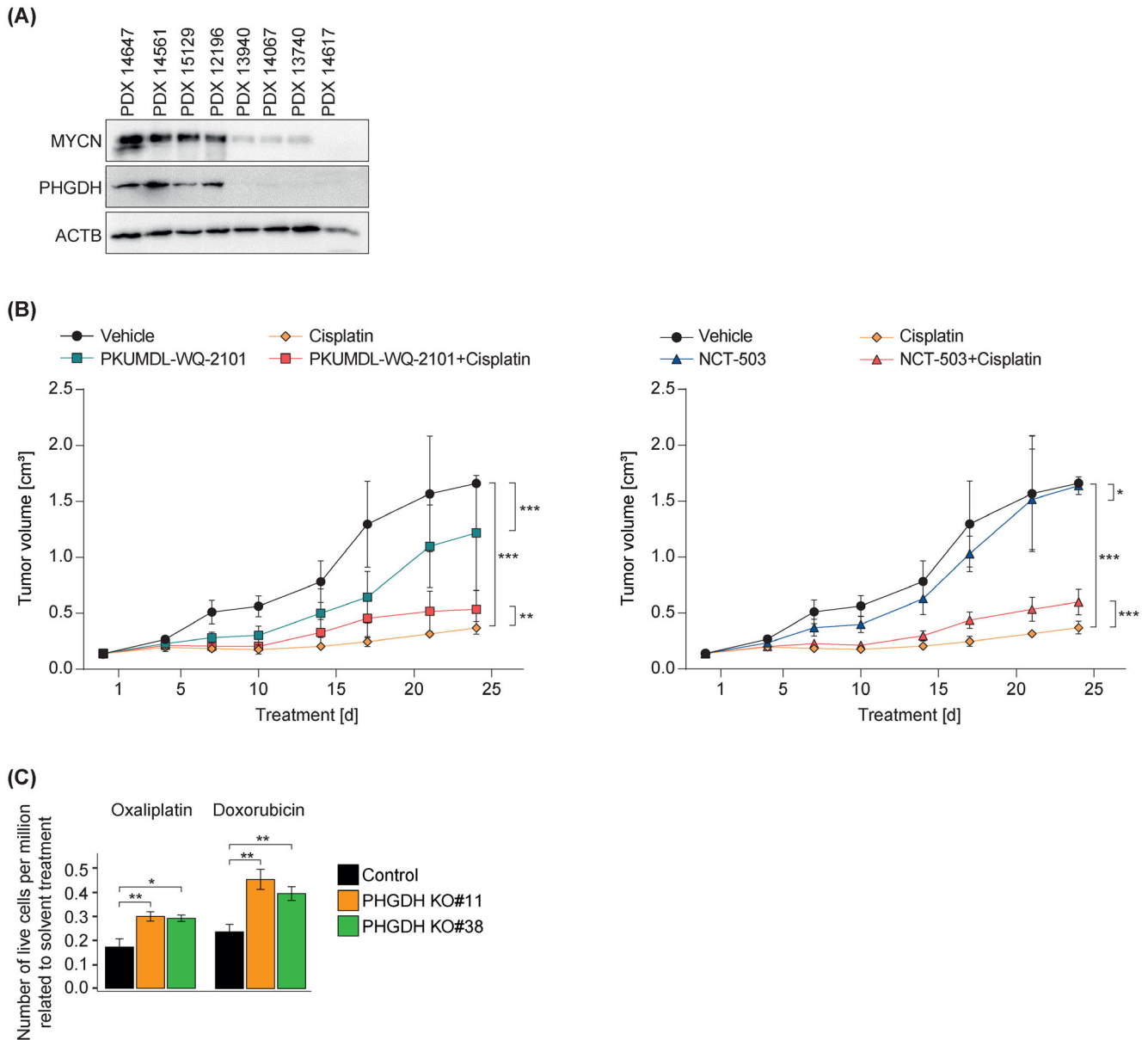


**FIGURE 4** PHGDH inhibitor treatment antagonizes chemotherapy efficacy in patient-derived xenografts in mice. A, Protein lysates were generated from eight patient-derived neuroblastoma xenografts established and propagated subcutaneously in mice. MYCN and PHGDH expression were investigated using western blotting.  $\beta$ -Actin served as loading control. B, Mean subcutaneous patient-derived xenograft (PDX) 14647 tumor volumes ( $\pm$ SD) are plotted over time from NOG mice ( $n = 4$ /study group) treated as indicated with combined vehicle control, 20 mg/kg/d PKUMDL-WQ-2101 ip daily (left graphics) or 40 mg/kg/d NCT-503 ip daily (right graphics), 1 mg/kg cisplatin iv weekly or a combination thereof. Treatment d 1 corresponds to d 20 of the PDX mouse experiment. C, Bars show the mean ( $\pm$ SD,  $n = 3$ ) number of live BE(2)-C PHGDH wildtype cells and PHGDH knockout clones #11 and #38 after treatment with 2  $\mu$ g/mL oxaliplatin or 0.05  $\mu$ g/mL doxorubicin for 96 hours normalized to the number of live cells of the respective solvent-treated controls. \* $P < .05$ , \*\* $P \leq .01$ , \*\*\* $P \leq .001$

induced a partial response in PDX 14647 while disease progressed under NCT-503 treatment.

Since targeted drugs would only be applied in concert with standard chemotherapy both in first-line and relapse therapy for MYCN-amplified neuroblastoma, which is categorized as high-risk disease, the PHGDH inhibitors were administered in 2-drug combination with cisplatin. Cisplatin is a standard-of-care chemotherapy drug in a wide spectrum of cancer types and major component of induction regimens

for children with high-risk neuroblastoma worldwide.<sup>37</sup> Drugs based on platinum are highly cytotoxic agents with the ability to damage DNA and inhibit DNA synthesis, consequently blocking mitosis and inducing apoptosis.<sup>38</sup> Cisplatin monotherapy for 25 days strongly inhibited PDX 14647 tumor growth in mice (mean tumor volumes: 349 mm<sup>3</sup>, cisplatin; 1661 mm<sup>3</sup>, vehicle; Figure 4B). Strikingly, either 2-drug combination with a PHGDH inhibitor was significantly less effective than cisplatin alone (Figure 4B), reducing mean tumor

volumes only to 525 mm<sup>3</sup> (PKUMDL-WQ-2101/cisplatin) and 605 mm<sup>3</sup> (NCT-503/cisplatin). To control for potential off-target effects and/or weak PHGDH inhibition by the two small molecules used, we turned to the genetic models and treated CRISPR/Cas9 PHGDH knockout clones and their respective controls with clinically relevant doses of oxaliplatin *in vitro*. A significantly higher number of live cells under oxaliplatin therapy was observed in PHGDH knockout cells compared to controls (Figure 4C), prompting us to test the efficacy of a second chemotherapeutic drug, doxorubicin, also a standard-of-care drug for high-risk neuroblastoma therapy but having an independent molecular mode of action. Doxorubicin treatment also allowed a significantly higher fraction of the PHGDH knockout clones to remain alive compared to controls (Figure 4C). Our data strongly demonstrate that while genetically engineering PHGDH knockout and pharmaceutically targeting PHGDH slows proliferation, both methods fail to kill neuroblastoma cells. *In vivo*, these tumors are then able to establish resistance to classical chemotherapy and evade treatment.

## 4 | DISCUSSION

We identified a protein set including PHGDH involved in serine synthesis and one-carbon metabolism in an unbiased shotgun proteomics approach illuminating the proteome-wide effector level correlating with oncogenic MYCN levels in primary neuroblastomas and neuroblastoma cell lines. Subsequent serine- and glycine-starvation experiments demonstrated that MYCN amplification decoupled the cells' dependence on an exogenous serine and glycine supply. Targeting the rate-limiting enzyme in *de novo* serine synthesis by genetic knockout and small molecule-based inhibition stalled proliferation in the short-term, but contributed to resistance development that impaired efficacy of the standard treatment regimen.

Capturing the landscape of intratumor heterogeneity in neuroblastomas has major implications not only for our understanding of cancer pathogenesis and progression, but also for drug development and effective translation of novel targeted therapies into the clinic as stand-alone or combination therapies. Multiregion sequencing from the same high-risk neuroblastoma<sup>39,40</sup> revealed high-level spatial heterogeneity with individual samples having different dominant clones. Since intratumor genetic heterogeneity and clonal evolution have become established as the rule rather than the exception in high-risk disease, the need to use preclinical models better recapitulating these traits has become more apparent. Xenografting patient samples may present an interesting approach to reflect intratumor heterogeneity as patient-derived neuroblastoma xenografts were recently reported to maintain genetic, epigenetic, transcriptional and phenotypic stability and reflect aspects of spatial intratumor heterogeneity.<sup>41,42</sup> The majority of models currently used in neuroblastoma research are monoclonal cell lines established decades ago and propagated as monolayer cultures and xenografts in mice. We have established eight neuroblastoma patient-derived xenografts that are passaged in mice (unpublished own data), which can be used to validate potential drug targets. Using this panel of PDXs, we show that expression of the

pacemaker enzyme in *de novo* serine synthesis, phosphoglycerate dehydrogenase, strongly correlates with MYCN oncogene expression, thereby confirming the data obtained in cell lines by Xia et al.<sup>43</sup> Strikingly, PHGDH inhibition by two well-characterized structurally divergent small molecule inhibitors<sup>34,35</sup> had only partial efficacy in monotherapy to stop neuroblastoma PDX tumor growth according to RECIST criteria<sup>36</sup> when tested in mice. Our data suggest that the anti-tumor effect by either drug is stronger within the first 14 days of treatment. Our results correspond with the efficacy that Xia et al achieved in BE(2)-C-xenografts in mice after 10 days of NCT-503 treatment,<sup>43</sup> which led them to conclude that PHGDH is a bona fide target in neuroblastoma cells, which when targeted, reduced tumor volumes and improved survival in their mouse cohort.<sup>43</sup> In our opinion, these diverging conclusions emphasize the need to ideally test therapeutic efficacy in *in vivo* disease models for longer time windows to capture the potential for reductions in efficacy that could be caused by or lead to resistance development to one or more drug in the clinical therapeutic picture and better mirror the patient situation. Our data is in line with findings by Chen et al, who performed a PHGDH knockdown in estrogen receptor-negative breast cancer xenograft models, and did not observe an effect on tumor maintenance and cell growth *in vivo* although cell proliferation and endogenous serine synthesis were impaired in breast cancer cell lines *in vitro*.<sup>44</sup> A study by DeNicola et al<sup>45</sup> reports reduced tumor growth by PHGDH knockdown in xenografted non-small cell lung cancer cells in mice, suggesting that the phenotypic consequences of PHGDH inhibition or knockdown vary among cancer entities as shown for a plethora of other drug targets.

All studies investigating PKUMDL-WQ-2101 and NCT-503 anti-tumor efficacy were performed to date with xenografted tumor cell lines in mice. Average serine concentrations in standard DMEM and RPMI 1640 media for cell culture are ~300-400  $\mu$ M according to manufacturer specifications. Physiological serine concentrations in human blood vary between 77 and 178  $\mu$ M in children 3 months to 6 years of age<sup>46</sup> and average 173.2  $\mu$ M  $\pm$  51.3 in adults.<sup>47</sup> In mice, circulating physiological serine concentrations average 161.8  $\mu$ M  $\pm$  14.0.<sup>48</sup> Consequently, cell lines are supplied with up to 4-fold higher serine concentrations *in vitro* than both in the patient and mice used in a preclinical *in vivo* model. Transplantation of cell lines from cell culture into mice transfers them from an artificially serine-rich to a physiological serine-poor environment. We observed upregulation of *de novo* serine synthesis and an induction of metabolic reprogramming upon serine and glycine depletion *in vitro*. Eventually, this metabolic reprogramming should also take place when cell lines are transplanted into mice, resulting in a higher vulnerability to metabolic intervention such as PHGDH inhibition for at least a short window of time, and possibly partially responsible for the observed success of the inhibitor in short-term testing in mice. Thus, suppressing PHGDH activity or downregulating PHGDH transcription may have different effects in xenografted cell lines compared to patient-derived xenografts, which are maintained by serial transfer in mice and never exposed or adapted to high-serine medium concentrations.

Tumor cells exist within a microenvironment shared with cancer-associated fibroblasts, immune and endothelial cells and biologically

active matrix molecules, from which the tumor cells receive influences that can promote tumor cell proliferation. Cellular metabolism is not only shaped by genetic factors such as *MYCN* amplification, but also by environmental factors such as local nutrient environment and distinct extracellular signaling events.<sup>49</sup> Xiao et al recently analyzed metabolic gene expression profiles in ~9000 single cells derived from melanomas and squamous cell carcinomas of the head and neck.<sup>50</sup> They found that metabolic features of single cancer cells are poorly captured by measurements performed on bulk tumors. Metabolic pathway activity in tumor cells appeared to be more plastic than that of normal cells in the tumor microenvironment, which have distinct metabolic features differing from tumor cells.<sup>50</sup> At this stage, one can only speculate that metabolic flux and absolute metabolite quantities regulated in part through the tumor microenvironment are better reflected in PDXs than xenografted cell lines or cultured cells. The resolution of emerging single-cell technology could illuminate fine circuitry provided by individual cells.

Worrisome from a translational viewpoint, is our observation obtained both in PDXs in mice and in vitro analyses in PHGDH knockout clones that pharmacological inhibition or genetic PHGDH knockout renders neuroblastoma cells resistant to standard-of-care chemotherapeutic drugs with undoubted importance for high-risk neuroblastoma therapy. As this conclusion is based on well-controlled settings from two different model systems, two different PHGDH inhibitors and two different chemotherapeutic drugs, we are called to proceed cautiously. We know that slowly proliferating cells are considerably less susceptible to chemotherapeutic intervention than rapidly proliferating cells from decades of cancer drug testing and clinical observation. In this regard, our in vitro data on cell viability were a first indication that single-agent PHGDH inhibitor therapy might slow proliferation but not kill the neuroblastoma cell. Nevertheless, only combining the PHGDH inhibitors with chemotherapy drugs in vivo and testing chemotherapy efficacy in the genetic knockout model allowed us to decipher this clinically important novel aspect. Data from pancreatic ductal adenocarcinoma cells, patient-derived xenografts and genetically engineered mice with *Kras* G12V and *Cdkn2a*-null mutations frequently observed in pancreatic ductal carcinoma show that sequential treatment with cyclin-dependent kinase inhibitors directly following taxanes proved capable of preventing cellular proliferation.<sup>51</sup> Sequentially administered PHGDH inhibitors and chemotherapeutic drugs should be tested in patient-derived neuroblastoma xenografts in mice in further studies to support the best possible design before combination is ruled out entirely for patients with *MYCN*-amplified neuroblastoma. Here we present data significantly correlating high-level *MYCN* to the expression of proteins important for de novo serine synthesis and one-carbon metabolism in neuroblastoma cells. *MYCN*-amplified cells shunt more carbons through de novo serine synthesis than cells harboring only the normal diploid *MYCN* complement, and both can restore their intracellular serine pools under serine and glycine deprivation although mechanisms in the *MYCN*-amplified cell are more effective. PHGDH knockout in *MYCN*-amplified cell lines has phenotypic consequences toward a more benign tumor biology, and these data fully justify the hypothesis that PHGDH serves as a

metabolic drug target. However, stand-alone therapy is not supported by the experimental evidence from longer-term testing in patient-derived neuroblastoma models in mice. Most importantly, reducing PHGDH activity renders neuroblastoma cells resistant to cytotoxic therapy. Based on the data presented in our study and unless substantial further testing in PDX mouse models proves that sequential administration eliminates antagonism of chemotherapy efficacy, we do not recommend to incorporate PHGDH small molecule inhibitors into treatment regimens for *MYCN*-amplified neuroblastoma.

## ACKNOWLEDGMENTS

The authors thank the German Neuroblastoma Biobank for providing primary tumor material, the Core Unit Immunopathology for Experimental Models at the Charité for providing immunohistochemistry services and Jenny Grobe (BIMSB at MDC) for technical assistance. This work was supported by the Berlin Institute of Health through CRG TERMINATE-NB (1.1.4.4, 53010045) to Hedwig E. Deubzer, Johannes H. Schulte and Angelika Eggert and a translational PhD project grant to Hedwig E. Deubzer and Stefan Kempa, by the German Cancer Aid through ENABLE (70112951, AVD 1233336) to Hedwig E. Deubzer, Stefan Kempa, Johannes H. Schulte and Angelika Eggert and by the German Cancer Consortium (DKTK) partner site Berlin to Hedwig E. Deubzer. Open Access funding enabled and organized by ProjektDEAL.

## CONFLICT OF INTEREST

The authors declare no competing interests.

## DATA AVAILABILITY STATEMENT

The mass spectrometry proteomics data have been deposited to the ProteomeXchange Consortium via the PRIDE partner repository with the dataset identifier PXD018300. The metabolomics data are available as Supporting Information. Other data will be made available upon request.

## ETHICS STATEMENT

Tumor samples were available from neuroblastoma patients in the NB2004 trial (NCT03042429; sponsor: University of Cologne), and informed consent was obtained. All animal experiments were performed in accordance with the "Guidelines for accommodation and care of laboratory animals" by the Council of Europe, and the protocol was approved by the local institutional ethics commission for animal experimentation.

## ORCID

Birte Arlt  <https://orcid.org/0000-0002-6665-4037>

Hedwig E. Deubzer  <https://orcid.org/0000-0002-6115-4893>

## REFERENCES

- Berthold F, Spix C, Kaatsch P, Lampert F. Incidence, survival, and treatment of localized and metastatic neuroblastoma in Germany 1979-2015. *Paediatr Drugs*. 2017;19:577-593.
- Brodeur GM. Neuroblastoma: biological insights into a clinical enigma. *Nat Rev Cancer*. 2003;3:203-216.
- Simon T, Hero B, Schulte JH, et al. 2017 GPOH guidelines for diagnosis and treatment of patients with neuroblastic tumors. *Klinische Pädiatrie*. 2017;229:147-167.

4. Valteau-Couanet D, Schleiermacher G, Sarnacki S, Pasqualini C. High-risk neuroblastoma treatment strategy: the experience of the SIOPEN group. *Bull Cancer*. 2018;105:918-924.
5. Keyel ME, Reynolds CP. Spotlight on dinutuximab in the treatment of high-risk neuroblastoma: development and place in therapy. *Biol Targets Ther*. 2019;13:1-12.
6. Matthay KK, Maris JM, Schleiermacher G, et al. Neuroblastoma. *Nat Rev Dis Primers*. 2016;2:16078.
7. Brodeur GM, Seeger RC, Schwab M, Varmus HE, Bishop JM. Amplification of N-myc in untreated human neuroblastomas correlates with advanced disease stage. *Science (New York, NY)*. 1984;224:1121-1124.
8. Peifer M, Hertwig F, Roels F, et al. Telomerase activation by genomic rearrangements in high-risk neuroblastoma. *Nature*. 2015;526:700-704.
9. Maris JM, Hogarty MD, Bagatell R, Cohn SL. Neuroblastoma. *Lancet*. 2007;369:2106-2120.
10. Schwab M, Alitalo K, Varmus HE, Bishop JM, George D. A cellular oncogene (c-Ki-ras) is amplified, overexpressed, and located within karyotypic abnormalities in mouse adrenocortical tumour cells. *Nature*. 1983;303:497-501.
11. Schwab M, Varmus HE, Bishop JM, et al. Chromosome localization in normal human cells and neuroblastomas of a gene related to c-myc. *Nature*. 1984;308:288-291.
12. Westermann F, Muth D, Benner A, et al. Distinct transcriptional MYCN/c-MYC activities are associated with spontaneous regression or malignant progression in neuroblastomas. *Genome Biol*. 2008;9:R150.
13. Schulte JH, Horn S, Otto T, et al. MYCN regulates oncogenic MicroRNAs in neuroblastoma. *Int J Cancer*. 2008;122:699-704.
14. Lee JW, Son MH, Cho HW, et al. Clinical significance of MYCN amplification in patients with high-risk neuroblastoma. *Pediatr Blood Cancer*. 2018;65:e27257.
15. Whitfield JR, Beaulieu ME, Soucek L. Strategies to inhibit Myc and their clinical applicability. *Front Cell Dev Biol*. 2017;5:10.
16. Lutz W, Stohr M, Schurmann J, Wenzel A, Lohr A, Schwab M. Conditional expression of N-myc in human neuroblastoma cells increases expression of alpha-prothymosin and ornithine decarboxylase and accelerates progression into S-phase early after mitogenic stimulation of quiescent cells. *Oncogene*. 1996;13:803-812.
17. Castro F, Dirks WG, Fahrnich S, Hotz-Wagenblatt A, Pawlita M, Schmitt M. High-throughput SNP-based authentication of human cell lines. *Int J Cancer*. 2013;132:308-314.
18. Rappsilber J, Mann M. Analysis of the topology of protein complexes using cross-linking and mass spectrometry. *CSH Protoc*. 2007;pdb prot4594.
19. Cox J, Mann M. MaxQuant enables high peptide identification rates, individualized p.p.b.-range mass accuracies and proteome-wide protein quantification. *Nat Biotechnol*. 2008;26:1367-1372.
20. Bielow C, Mastrobuoni G, Kempa S. Proteomics quality control: quality control software for MaxQuant results. *J Proteome Res*. 2016;15:777-787.
21. Tyanova S, Temu T, Sinitcyn P, et al. The Perseus computational platform for comprehensive analysis of (prote)omics data. *Nat Methods*. 2016;13:731-740.
22. Cox J, Mann M. 1D and 2D annotation enrichment: a statistical method integrating quantitative proteomics with complementary high-throughput data. *BMC Bioinform*. 2012;13(suppl 16):S12.
23. R Core Team. *R: A Language and Environment for Statistical Computing*. Vienna, Austria: R Foundation for Statistical Computing; 2018. <https://www.R-project.org/>.
24. Kempa S, Hummel J, Schwemmer T, et al. An automated GCxGC-TOF-MS protocol for batch-wise extraction and alignment of mass isotopomer matrixes from differential <sup>13</sup>C-labelling experiments: a case study for photoautotrophic-mixotrophic grown *Chlamydomonas reinhardtii* cells. *J Basic Microbiol*. 2009;49:82-91.
25. Kováts E. Gas-chromatographische Charakterisierung organischer Verbindungen. Teil 1: Retentionsindices aliphatischer Halogenide, Alkohole, Aldehyde und Ketone. *Helv Chim Acta*. 1958;41(7):1915-1932.
26. Kuich PH, Hoffmann N, Kempa S. Maui-VIA: a user-friendly software for visual identification, alignment, correction, and quantification of gas chromatography-mass spectrometry data. *Front Bioeng Biotechnol*. 2014;2:84.
27. Lorkiewicz P, Higashi RM, Lane AN, Fan TW. High information throughput analysis of nucleotides and their isotopically enriched isotopologues by direct-infusion FTICR-MS. *Metabolomics*. 2012;8:930-939.
28. Lodrini M, Sprussel A, Astrahantseff K, et al. Using droplet digital PCR to analyze MYCN and ALK copy number in plasma from patients with neuroblastoma. *Oncotarget*. 2017;8:85234-85251.
29. Benjamini YHY. Controlling the false discovery rate: a practical and powerful approach to multiple testing. *J R Stat Soc Ser B*. 1995;57(1):289-300.
30. R Core Team. *R: A Language and Environment for Statistical Computing*. Vienna, Austria: R Foundation for Statistical Computing; 2019. <https://www.R-project.org/>.
31. Hsu CL, Chang HY, Chang JY, Hsu WM, Huang HC, Juan HF. Unveiling MYCN regulatory networks in neuroblastoma via integrative analysis of heterogeneous genomics data. *Oncotarget*. 2016;7:36293-36310.
32. Yang M, Vousden KH. Serine and one-carbon metabolism in cancer. *Nat Rev Cancer*. 2016;16:650-662.
33. Mattaini KR, Sullivan MR, Vander Heiden MG. The importance of serine metabolism in cancer. *J Cell Biol*. 2016;214:249-257.
34. Wang Q, Liberti MV, Liu P, et al. Rational design of selective allosteric inhibitors of PHGDH and serine synthesis with anti-tumor activity. *Cell Chem Biol*. 2017;24:55-65.
35. Pacold ME, Brimacombe KR, Chan SH, et al. A PHGDH inhibitor reveals coordination of serine synthesis and one-carbon unit fate. *Nat Chem Biol*. 2016;12:452-458.
36. Schwartz LH, Litiere S, de Vries E, et al. RECIST 1.1-update and clarification: from the RECIST committee. *Eur J Cancer (Oxford, England: 1990)*. 2016;62:132-137.
37. Dilruba S, Kalayda GV. Platinum-based drugs: past, present and future. *Cancer Chemother Pharmacol*. 2016;77:1103-1124.
38. Kelland L. The resurgence of platinum-based cancer chemotherapy. *Nat Rev Cancer*. 2007;7:573-584.
39. Chicard M, Colmet-Daage L, Clement N, et al. Whole-exome sequencing of cell-free DNA reveals temporo-spatial heterogeneity and identifies treatment-resistant clones in neuroblastoma. *Clin Cancer Res*. 2018;24:939-949.
40. Bellini A, Bernard V, Leroy Q, et al. Deep sequencing reveals occurrence of subclonal ALK mutations in neuroblastoma at diagnosis. *Clin Cancer Res*. 2015;21:4913-4921.
41. Braekeveldt N, von Stedingk K, Fransson S, et al. Patient-derived xenograft models reveal Intratumor heterogeneity and temporal stability in neuroblastoma. *Cancer Res*. 2018;78:5958-5969.
42. Brabetz S, Leary SES, Grobner SN, et al. A biobank of patient-derived pediatric brain tumor models. *Nat Med*. 2018;24:1752-1761.
43. Xia Y, Ye B, Ding J, et al. Metabolic reprogramming by MYCN confers dependence on the serine-glycine-one-carbon biosynthetic pathway. *Cancer Res*. 2019;79:3837-3850.

44. Chen J, Chung F, Yang G, et al. Phosphoglycerate dehydrogenase is dispensable for breast tumor maintenance and growth. *Oncotarget*. 2013;4:2502-2511.
45. DeNicola GM, Chen PH, Mullarky E, et al. NRF2 regulates serine biosynthesis in non-small cell lung cancer. *Nat Genet*. 2015;47:1475-1481.
46. van Karnebeek CD, Shevell M, Zschocke J, Moeschler JB, Stockler S. The metabolic evaluation of the child with an intellectual developmental disorder: diagnostic algorithm for identification of treatable causes and new digital resource. *Mol Genet Metab*. 2014;111:428-438.
47. Psychogios N, Hau DD, Peng J, et al. The human serum metabolome. *PLoS One*. 2011;6:e16957.
48. Rivera S, Lopez-Soriano FJ, Azcon-Bieto J, Argiles JM. Blood amino acid compartmentation in mice bearing Lewis lung carcinoma. *Cancer Res*. 1987;47:5644-5646.
49. Palm W, Thompson CB. Nutrient acquisition strategies of mammalian cells. *Nature*. 2017;546:234-242.
50. Xiao Z, Dai Z, Locasale JW. Metabolic landscape of the tumor microenvironment at single cell resolution. *Nat Commun*. 2019;10:3763.
51. Salvador-Barbero B, Álvarez-Fernández M, Zapatero-Solana E, et al. CDK4/6 inhibitors impair recovery from cytotoxic chemotherapy in pancreatic adenocarcinoma. *Cancer Cell*. 2020;37:340-353.

#### SUPPORTING INFORMATION

Additional supporting information may be found online in the Supporting Information section at the end of this article.

**How to cite this article:** Arlt B, Zasada C, Baum K, et al. Inhibiting phosphoglycerate dehydrogenase counteracts chemotherapeutic efficacy against MYCN-amplified neuroblastoma. *Int. J. Cancer*. 2021;148:1219–1232. <https://doi.org/10.1002/ijc.33423>